Control of Transient Power During Unintentional Islanding of Microgrids

Walid R. Issa, Mohammad A. Abusara, and Suleiman M. Sharkh, *Member, IEEE*

***Abstract*—In inverter-based microgrids, the paralleled inverters need to work in grid-connected mode and stand-alone mode and to transfer seamlessly between the two modes. In grid-connected mode, the inverters control the amount of power injected into the grid. In stand-alone mode, however, the inverters control the island voltage while the output power is dictated by the load. This can be achieved using the droop control. Inverters can have different power set points during grid-connected mode, but in stand-alone mode, they all need their power set points to be adjusted according to their power ratings. However, during sudden unintentional islanding (due to loss of mains), transient power can flow from inverters with high power set points to inverters with low power set points, which can raise the dc-link voltage of the inverters causing them to shut down. This paper investigates the transient circulating power between paralleled inverters during unintentional islanding and proposes a controller to limit it. The controller monitors the dc-link voltage and adjusts the power set point in proportion to the rise in the voltage. A small-signal model of an islanded microgrid is developed and used to design the controller. Simulation and experimental results are presented to validate the design.**

***Index Terms*—Droop control, microgrid, power sharing, unintentional islanding.**

NOMENCLATURE

P^*, Q^*	Active and reactive power set points.
P, Q	Instantaneous active and reactive power.
R	Load resistance.
X	Inverter output inductance.
k_ω, k_a	Frequency and voltage drooping gains.
V_o, ω_o	Voltage and frequency set points.
τ	Measurement filter time constant.
V^*_{DClink}	Nominal dc-link voltage.
C_{dc}	dc-link capacitor.
$V_{\mathrm{eq}}, \theta_{\mathrm{eq}}$	Voltage and phase equilibrium points.

I. INTRODUCTION

THE concept of the microgrid has emerged in response to the increased penetration of renewable energy systems. In a microgrid, distributed generation (DG) units, energy storage systems (ESSs), and loads are aggregated as one unit connected to the grid via a static transfer switch (STS), as illustrated in Fig. 1. Due to their controllability, microgrids will become the building blocks of future smart grids. Compared to a single DG unit, a microgrid has more capacity and control flexibility, which can improve system reliability and power quality. A microgrid can operate in grid-connected mode or in stand-alone mode. In grid-connected mode, DG units can export power to the grid (when the price is advantageous, for example) or import power and store it in the ESS for later use. During a power outage, the microgrid works autonomously and provides power to local load. The ESS can be used to balance any mismatch between load demand and the power available from renewable sources. To avoid the power supply interruption, it is necessary for the microgrid to be able to transfer seamlessly from grid-connected mode to island mode and vice versa. Low-speed communication between the supervisory controller and all units can be also used for the power management and monitoring beside decision-making outcomes transfer.

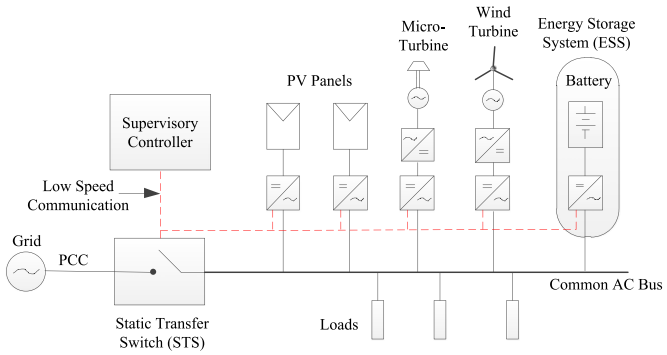

Fig. 1. Microgrid structure.

There are a number of publications on the control of grid interactive PWM inverters [1]–[7]. Chandorkar *et al*. [8] proposed a grid interactive PWM inverter based on P-ω and Q-V droop control where the inverter frequency and voltage amplitude are drooped linearly with the inverter output active and reactive power, respectively. Inverters can operate in parallel and load sharing is achieved without the need for communication signals between the inverters.

Using droop control, it is possible for the inverter to transfer from the grid-connected mode to the stand-alone mode seamlessly [11]. During grid-connected mode, the frequency is stiff and maintained by the power grid. Hence, the power set point of the droop controller can be used to control the power output of the inverter. This power set point can be adjusted by an energy management system implemented inside the supervisory controller. In stand-alone mode, however, the frequency can

Manuscript received March 3, 2014; revised May 26, 2014 and September 2, 2014; accepted September 9, 2014. Date of publication September 23, 2014; date of current version March 5, 2015. Recommended for publication by Associate Editor M. Liserre.

W. R. Issa and M. A. Abusara are with the Renewable Energy Research Group, College of Engineering, Mathematics, and Physical Sciences, University of Exeter, Cornwall Campus, Penryn TR10 9EZ, U.K. (e-mail: wrmi201@exeter.ac.uk; m.abusara@exeter.ac.uk).

S. M. Sharkh is with the Electro-Mechanical Engineering Research Group, Faculty of Engineering and the Environment, University of Southampton, Highfield Campus, Southampton SO17 1BJ, U.K. (e-mail: suleiman@soton.ac.uk).

Color versions of one or more of the figures in this paper are available online at http://ieeexplore.ieee.org.

Digital Object Identifier 10.1109/TPEL.2014.2359792

deviate from its nominal value depending on the amount of power drawn by the local load and the power set point can be used to reduce this deviation.

In the case of multiple inverters operating in stand-alone mode, each set point has to be adjusted according to the power rating of the inverter, i.e., according to the drooping gain. Therefore, the power set point has two different purposes depending on the mode of operation: 1) in grid-connected mode, power set point is set to control the output power; and 2) in stand-alone mode, it is used to reduce the frequency deviation. Before changing from grid-connected to stand-alone mode, the supervisory controller needs to bring all the power set points of all paralleled inverters to their nominal values before disconnecting from the grid. However, if unintentional islanding occurs, it is not possible to adjust the power set points to match the load demand instantaneously. As a result circulating power can flow from the inverters with higher power set points to inverters with lower set points. It is important to note that by using the common antiislanding strategy, the period from grid failure until the opening of the STS may vary depending on the mismatch between the power generated by the microgrid and the local distributed load. If the mismatch is large, islanding detection will be quite quick. However, if the mismatch is small, it will take longer for the antiislanding controller to detect grid power loss. In the worst case scenario of perfect mismatch between the power generated and the load, the antiislanding controller should not take more than 2 s according to the IEEE Standard 1547 [10]. If one inverter imports power during this period, the dc-link voltage will rise and might exceed the maximum limit. This will cause the inverter to shut down to prevent damage. Even though there has been a number of publications recently on seamless transfer of microgrids [9], [11], [12], the effect of different power set points on the transient power between inverters has not yet been discussed.

This paper investigates the issue of transient power between parallel inverters during unintentional islanding. This circulating power can raise the dc-link voltage of the inverters causing the inverter to shut down if the voltage level exceeds its maximum limit. This paper also proposes a controller to limit this circulating power by adjusting the power set point according to the rise in the dc-link voltage. A small-signal model of a microgrid consisting of two inverters in island mode is developed and used to design the controller. Simulation and experimental results are presented to validate the design. The main contributions of this paper are: 1) analysis of a microgrid during unintentional islanding and the effect of this on the dc-link voltage; 2) using small-signal perturbation to develop a model of an island microgrid of two parallel-connected inverters; and 3) the design of a controller that limits the rise of the dc-link voltage during unintentional islanding.

The rest of this paper is organized as follows. Section II discusses the droop control operation and analysis of unintentional islanding. Section III presents a small-signal model of a microgrid consisting of two inverters. The proposed controller is presented in Section IV. Simulation and Experimental results are presented in Section V.

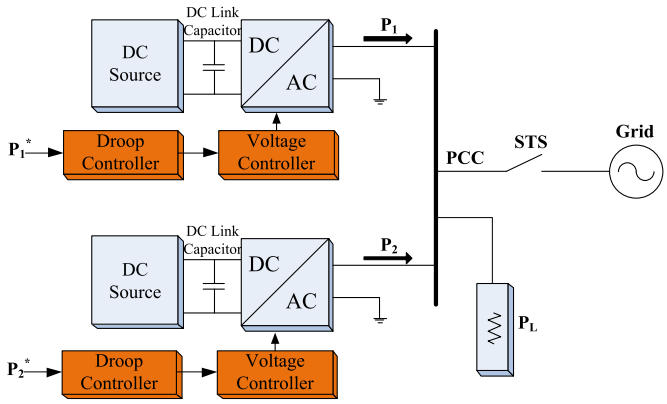

Fig. 2. Two inverters in microgrid.

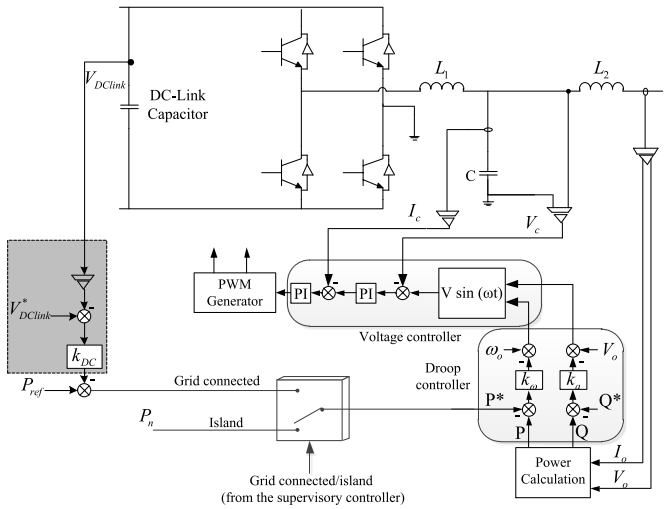

Fig. 3. Inverter circuit diagram.

TABLE I
DC/AC CONVERTER PARAMETER VALUES

Symbol	Value	Description
L_1	1350 μH	Inverter-side filter inductor
C	240 μF	Filter capacitor
L_2	300 μH	Grid-side filter inductor
C_{dc}	2000 μF	DC-link capacitor

II. DROOP CONTROL

In this paper, a microgrid consisting of two inverters as shown in Fig. 2 is considered. The circuit diagram of each inverter and its *LCL* filter and controller is illustrated in Fig. 3. The system parameters are listed in Table I. The frequency and voltage droop control laws of an inverter operating in a microgrid is given by

$$\omega = \omega_o^* - k_\omega (P - P^*) \tag{1}$$

$$V = V_o^* - k_a (Q - Q^*) \tag{2}$$

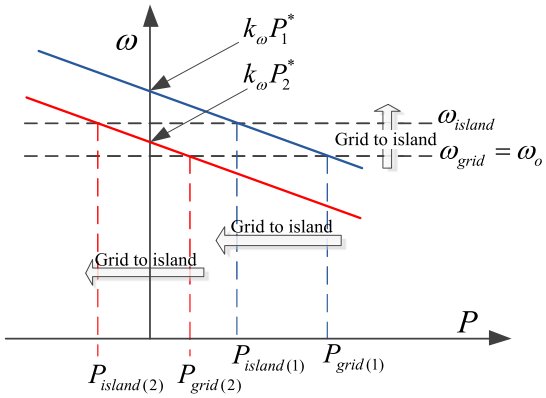

Fig. 4. Droop control of two inverters in microgrid.

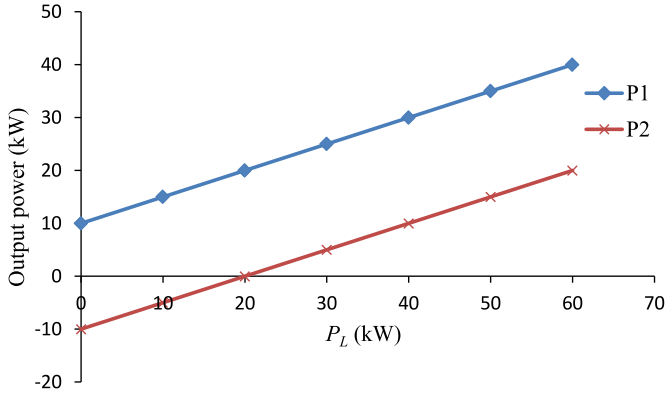

Fig. 5. Output power versus load power. $P_1^* = 30$ kW, $P_2^* = 10$ kW.

where ω_o^* and V_o^* are the nominal frequency and nominal voltage references, k_ω and k_a are the frequency proportional drooping coefficient and voltage proportional drooping coefficient, respectively. The droop slopes are determined according to the power rating of the inverter and according to the maximum allowable variations in the output frequency and voltage [13]. In grid-connected mode, the active and reactive power set points P^* and Q^* are adjusted to be equal to the reference power values, $P_{\rm ref}$ and $Q_{\rm ref}$. In stand-alone mode, however, they are set to nominal active and reactive power values, P_n and Q_n, to improve the frequency and voltage regulation [11]. The inverter controller receives a signal from the supervisory controller about the status of the STS, and the set points P^* and Q^* are set accordingly as shown in Fig. 3.

Without losing generality, it is assumed that the two inverters in Fig. 2 have the same power ratings, and hence, they have the same drooping gains $k_{\omega_1} = k_{\omega_2} = k_\omega$. In grid-connected mode, the inverters are assumed to have different power set points such as $P_1^* \neq P_2^*$.

Fig. 4 shows the droop control of the two inverters with different power set points. During grid-connected mode, the frequency is fixed by the stiff grid to be $\omega_{\rm grid}$ that equals the nominal frequency ω_o and the two inverters generate different power values $P_{{\rm grid}(1)}$ and $P_{{\rm grid}(2)}$. When the microgrid transfers to island mode (due to unintentional islanding), the island frequency $\omega_{\rm island}$ deviates from its nominal value ω_o and inverters 1 and 2 generate $P_{{\rm island}(1)}$ and $P_{{\rm island}(2)}$, respectively. In this case, $P_{{\rm island}(2)}$ is negative, and hence, inverter 2 is importing power. In the event of unintentional islanding and from (1), the system will reach as steady-state frequency value of

$$\begin{aligned}\omega_{\rm island} &= \omega_o^* - k_{\omega 1}P_1 + k_{\omega 1}P_1^* \\ &= \omega_o^* - k_{\omega 2}P_2 + k_{\omega 2}P_2^*. \end{aligned} \tag{3}$$

Knowing that the two inverters have the same drooping gain $k_{\omega 1} = k_{\omega 2} = k_\omega$, (3) leads to

$$P_1 = P_1^* + P_2 - P_2^*. \tag{4}$$

The total power dissipated by the load should equal the output power generated by the two inverters, i.e.,

$$P_L = P_1 + P_2. \tag{5}$$

Substituting (4) and (5) into (3), the steady-state island frequency is given by

$$\omega_{\rm island} = \omega_o^* - \frac{k_\omega}{2}(P_L - P_1^* - P_2^*). \tag{6}$$

The aforementioned equation shows that the deviation from the nominal frequency depends on the local load and the power set points of the inverters. Substituting (5) into (4), the steady-state output power of inverter 1 in island mode is given by

$$P_1 = \frac{1}{2}(P_L + P_1^* - P_2^*). \tag{7}$$

Similarly, the steady-state output power of inverter 2 is given by

$$P_2 = \frac{1}{2}(P_L + P_2^* - P_1^*). \tag{8}$$

Equations (7) and (8) show that the two inverters will only share the load equally if $P_1^* = P_2^*$. They also show that if the load power is less than the difference between the two set points, i.e.,

$$P_L < |P_1^* - P_2^*| \tag{9}$$

then one of the inverters will import power. Consider, for example, the case where $P_1^* = 30\,{\rm kW}$ and $P_2^* = 10\,{\rm kW}$, Fig. 5 shows how the inverters output power varies with respect to local load. If islanding happens when the load is less than 20 kW, i.e.,$P_L < P_1^* - P_2^*$, the power output P_2 will be negative, hence, inverter 2 will import power. This power will cause the dc-link voltage (see Fig. 3) to rise and if the voltage exceeds the maximum allowed limit, the inverter will shut down. This phenomenon will reduce the reliability of the microgrid. In normal operation and after unintentional islanding is detected by the supervisory controller, a signal is sent to all inverters updating them with the status of the microgrid (grid-connected or stand-alone) so that the inverters local controller changes the set points. However, this signal is sent via a relatively slow communication protocol (such as CAN-bus or Ethernet).

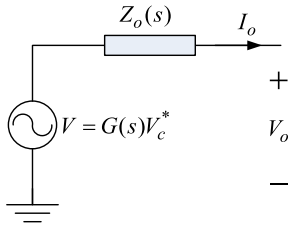

Fig. 6. Inverter equivalent circuit.

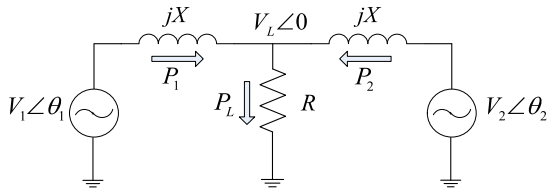

Fig. 7. Equivalent circuit of two inverters in island mode.

Regardless of the speed of the communication protocol, there can be some delay between when the islanding happens and until islanding is detected by the supervisory controller and an update signal is sent and received. During this transitional period, the dynamic of the microgrid is important in determining the amount of energy imported by an inverter.

III. Small-Signal Model

In this section, a small-signal model is developed to analyze the system's behavior during unintentional islanding. The model will be developed for two inverters in island mode. An inverter can be modeled by a two-terminal Thevenin equivalent circuit as shown in Fig. 6, where $G(s)$ and $Z_o(s)$ represent the closed-loop and output impedance transfer functions, respectively [14]. The response time of $G(s)$ is quite fast with respect to that of the outer droop control, and hence, it will be assumed as unity [11].

The output impedance $Z_o(s)$ is predominantly inductive around the fundamental frequency [4], [5], [14], and hence, $Z_o(s)$ can be approximated such as $Z_o(s) \approx sL_o$. The inductance L_o can be determined by the slope of $Z_o(s)$ around the fundamental frequency, and in the experimental setup used in this paper, it is 2500 μH. Fig. 7 shows the equivalent circuit for the two inverters operating in island mode. For simplicity, it is assumed that both inverters have identical output impedance $X = \omega L_o$ and they supply a local resistive load.

A. Power Flow Equations and Power Measurement

The current that flows from each inverter can be described as follows:

$$I_n = \frac{V_n\angle\theta_n - V_L}{X\angle 90}, \quad n = 1, 2. \tag{10}$$

Applying the Kirchhoff current law at the load node gives

$$\frac{V_L - V_1\angle\theta_1}{X\angle 90} + \frac{V_L}{R} + \frac{V_L - V_2\angle\theta_2}{X\angle 90} = 0. \tag{11}$$

Rearranging (11), the load voltage is given by

$$V_L = \frac{R(V_1\angle\theta_1 + V_2\angle\theta_2)}{2R + X\angle 90}. \tag{12}$$

The apparent power of each inverter is given by

$$P_n + jQ_n = V_n \,.\, I_n^*, n = 1, 2. \tag{13}$$

Substituting (12) into (10) and the result into (13), the instantaneous active and reactive powers (in the time domain) for the two inverters are given by

$$P_1 = \frac{\frac{XV_1^2}{R} + 2V_1V_2\sin(\theta_1 - \theta_2) + \frac{XV_1V_2}{R}\cos(\theta_1 - \theta_2)}{4X + \frac{X^3}{R^2}} \tag{14}$$

$$Q_1 = \frac{\left(\frac{X^2}{R^2} + 2\right)V_1^2 - 2V_1V_2\cos(\theta_1 - \theta_2) + \frac{XV_1V_2}{R}\sin(\theta_1 - \theta_2)}{4X + \frac{X^3}{R^2}} \tag{15}$$

$$P_2 = \frac{\frac{XV_2^2}{R} + 2V_1V_2\sin(\theta_2 - \theta_1) + \frac{XV_1V_2}{R}\cos(\theta_2 - \theta_1)}{4X + \frac{X^3}{R^2}} \tag{16}$$

$$Q_2 = \frac{\left(\frac{X^2}{R^2} + 2\right)V_2^2 - 2V_1V_2\cos(\theta_2 - \theta_1) + \frac{XV_1V_2}{R}\sin(\theta_2 - \theta_1)}{4X + \frac{X^3}{R^2}}. \tag{17}$$

When practically implementing the droop control, average active and reactive powers need to be measured, and thus, the droop control equations described in (1) and (2) become

$$\omega = \omega_o^* - k_\omega(P_{\text{avg}} - P^*) \tag{18}$$

$$V = V_o^* - k_a(Q_{\text{avg}} - Q^*). \tag{19}$$

The average power can be obtained by passing the instantaneous powers through a low-pass filter (LPF) as it common and easier to be programmed in a DSP. Hence, the average power P_{avg}, and Q_{avg} in the s-domain, are given by

$$P_{\text{avg}} = F(s)P(s) \tag{20}$$

$$Q_{\text{avg}} = F(s)Q(s). \tag{21}$$

where $P(s)$ and $Q(s)$ are the instantaneous active power and reactive power, respectively, as described in (14)–(17). $F(s)$ is the transfer function of the LPF and is given by

$$F(s) = \frac{1}{\tau s + 1} \tag{22}$$

where τ is the filter time constant.

B. State-Space Equations

By perturbing the power flow equations (14)–(17), we obtain

$$\Delta P_1 = a_1\Delta V_1 + b_1\Delta V_2 + c_1\Delta\theta_1 + d_1\Delta\theta_2 \quad (23)$$

$$\Delta P_2 = a_2\Delta V_1 + b_2\Delta V_2 + c_2\Delta\theta_1 + d_2\Delta\theta_2 \quad (24)$$

$$\Delta Q_1 = a_3\Delta V_1 + b_3\Delta V_2 + c_3\Delta\theta_1 + d_3\Delta\theta_2 \quad (25)$$

$$\Delta Q_2 = a_4\Delta V_1 + b_4\Delta V_2 + c_4\Delta\theta_1 + d_4\Delta\theta_2. \quad (26)$$

where Δ means a small perturbation around the equilibrium points. The coefficients a, b, c, and d (with the different subscripts) are obtained by calculating the corresponding partial derivatives and they are given in Appendix A.

By perturbing (18) and (19), we obtain

$$\Delta\omega_n = -k_\omega\Delta P_{\mathrm{avg}n} \quad (27)$$

$$\Delta V_n = -k_a\Delta Q_{\mathrm{avg}n}. \quad (28)$$

Substituting (22) into (20) and (21), the average power is related to the instantaneous power by

$$\Delta P_{\mathrm{avg}n} = \frac{1}{\tau s+1}\Delta P_n \quad (29)$$

$$\Delta Q_{\mathrm{avg}n} = \frac{1}{\tau s+1}\Delta Q_n. \quad (30)$$

Substituting (23) into (29) and rearranging gives

$$s.\Delta P_{\mathrm{avg}n} = \frac{1}{\tau}\left(a_n\Delta V_1 + b_n\Delta V_2 + c_n\Delta\theta_1 + d_n\Delta\theta_2\right) - \frac{1}{\tau}\Delta P_{\mathrm{avg}n}, \quad n=1,2. \quad (31)$$

Substituting (25) into (30) and rearranging gives

$$s.\Delta Q_{\mathrm{avg}n} = \frac{1}{\tau}\left(a_{n+2}\Delta V_1 + b_{n+2}\Delta V_2 + c_{n+2}\Delta\theta_1 + d_{n+2}\Delta\theta_2\right) - \frac{1}{\tau}\Delta Q_{\mathrm{avg}n}, \quad n=1,2. \quad (32)$$

The inverter power angle is related to the frequency by

$$s\Delta\theta_n = \Delta\omega_n, \quad n=1,2. \quad (33)$$

Equations (23)–(33) can be combined into a homogenous state-space equation such as

$$[\mathrm{sX_1}] = [\mathrm{A_1}]\,[\mathrm{X_1}] \quad (34)$$

where $[\mathrm{X_1}]$ contains the state variables and is given by

$$[\mathrm{X_1}] = \begin{bmatrix} \Delta\theta_1 \\ \Delta\theta_2 \\ \Delta\omega_1 \\ \Delta\omega_2 \\ \Delta V_1 \\ \Delta V_2 \\ \Delta P_{\mathrm{avg}1} \\ \Delta P_{\mathrm{avg}2} \\ \Delta Q_{\mathrm{avg}1} \\ \Delta Q_{\mathrm{avg}2} \end{bmatrix}.$$

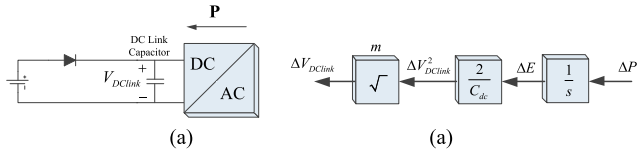

Fig. 8. DC-link capacitor (a) when dc/ac inverter is importing power, (b) small-signal model.

The state variable matrix $[\mathrm{A_1}]$ is given in Appendix B. Equation (34) represents a stats-space model of the two inverters in island mode.

IV. DC-Link Voltage Controller

A. DC-Link Modeling

As explained earlier, the imported power may raise the dc-link voltage to an unacceptable limit. In this section, the state-space model developed in Section III will be extended to include the dc-link voltage. Fig. 8(a) shows the dc-link capacitor when the inverter is importing power during the transient period. The energy E absorbed by the capacitor is related to the capacitor voltage V_{DClink} by

$$E = \int P(t)dt = \frac{1}{2}C_{\mathrm{dc}}V^2_{\mathrm{DClink}} \quad (35)$$

where P is the absorbed power and C_{dc} is the dc-link capacitance. In order to have a linear relationship between ΔP and V_{DClink}, the square-root relation needs to be linearized. Let $x = V^2_{\mathrm{DClink}}$ and $y(x) = \sqrt{x}$, a small change in y is given by

$$\Delta y = \Delta x\,.\,\frac{dy}{dx}\bigg|_{x=x_o} \quad (36)$$

where Δx is a small change in x and x_o is the equilibrium point. Given that the dc-link voltage needs to be around X_o, Δy becomes

$$\Delta y = m\,.\,\Delta x \quad (37)$$

where $m = \frac{dy}{dx}\Big|_{x=x_o} = \frac{1}{2\sqrt{x}}\Big|_{x=X_o^2}$.

Therefore, as shown in Fig. 8(b), the linear relationship between the dc-link voltage and the power is given by

$$\Delta V_{\mathrm{DClink}n} = \frac{2m}{C_{\mathrm{dc}}s}\,.\,\Delta P_n. \quad (38)$$

Substituting (23) and (24) into (38) gives the state equation for $\Delta V_{\mathrm{DClink1}}$ and $\Delta V_{\mathrm{DClink2}}$. This can then be integrated with (34) to give (39) such as

$$[\mathrm{sX_2}] = [\mathrm{A_2}]\,[\mathrm{X_2}] \quad (39)$$

where

$$[\mathrm{X_2}] = \begin{bmatrix} \mathrm{X_1} \\ \Delta V_{\mathrm{DClink1}} \\ \Delta V_{\mathrm{DClink2}} \end{bmatrix}$$

$$[\mathrm{A_2}] = \begin{bmatrix} \mathrm{A_1} & [0]_{10\times 2} \\ \mathrm{A_3} & [0]_{2\times 2} \end{bmatrix}.$$

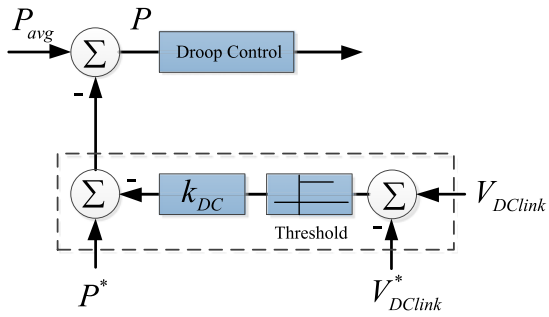

Fig. 9. Proposed controller based on the dc-link voltage.

A_3 is given in Appendix B.

Equation (39) represents the state-space equation for the complete model of the two inverters in island mode including the dynamics of the dc-link voltages.

B. Design of DC-Link Voltage Controller to Limit Transient Power

In this section, a controller is proposed to limit the amount of imported power during the transitional period, so the inverters carry on working without interruption until they receive the update signal from the supervisory controller as explained earlier. The controller reduces the power set points if the Dc-link voltage exceeds a certain limit. The proposed controller is illustrated in Fig. 9.

During normal operation when the power flows out of the inverter, the dc-link voltage is regulated by a dc/dc boost converter. The reference V^*_{DCLink} is the nominal dc voltage such that it only becomes effective if the dc-link voltage exceeds a threshold, which means the inverter is importing power. In this case, the controller will change the reference power set point until the dc voltage difference is minimized.

The controller gain k_{DC} must be selected carefully to guarantee good stability and good reduction in imported energy. In order to analyze stability, the small-signal model described by (39) will be slightly modified to include the dc-link voltage controller. If the proposed controller is implemented for inverter 1, then from Fig. 9, we can write

$$P_1 = P_{\mathrm{avg1}} - P^* + k_{\mathrm{DC}}(V_{\mathrm{DClink1}} - V^*_{\mathrm{DClink1}}). \tag{40}$$

By perturbing (40) around the equilibrium points, we get

$$\Delta P_1 = \Delta P_{\mathrm{avg1}} + k_{\mathrm{DC}} \Delta V_{\mathrm{DClink1}}. \tag{41}$$

Substituting (41) into (27) gives

$$\Delta\omega = -k_\omega(\Delta P_{\mathrm{avg1}} + k_{\mathrm{DC}} \Delta V_{\mathrm{DClink1}}). \tag{42}$$

The state variable "s. $\Delta\omega$" becomes

$$s\Delta\omega = -k_\omega s\Delta P_{\mathrm{avg1}} - k_\omega k_{\mathrm{DC}} s\Delta V_{\mathrm{DClink1}}. \tag{43}$$

The state-space equation of (39) can be modified to include this control loop. It can be done by modifying the third row of the state matrix of A_2 according to (43). If the controller is implemented for inverter 2, then the fourth row of A_2 is also modified.

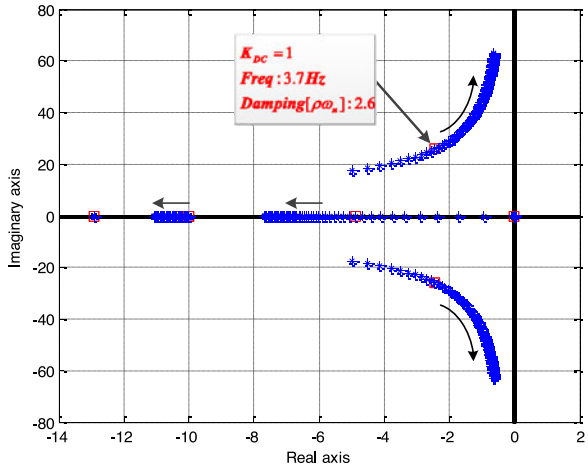

Fig. 10. Root locus of the system when $0 < k_{\mathrm{DC}} < 10$.

In order to analyze the effect of k_{DC} on the stability of the system, the locus of the eigenvalues of A_2 is plotted as shown in Fig. 10. The eigenvalues of the system are plotted for $0 < k_{\mathrm{DC}} < 10$. They are in the left half plane for the selected gain range. The arrows depict the evolution of the eigenvalues when the gain value increases, which show that the system becomes faster with higher overshoot by increasing the gain since the complex poles become the dominant poles, while the effect of the real poles decreases, which could result in the dc-link voltage exhibiting greater oscillations, and even, instability if the gain is increased further.

Increasing the gain k_{DC} decreases the absorbed energy and so the dc voltage is minimized. However, it will increase the oscillatory components resulting in higher overshoot. Thus, by choosing k_{DC} to 1, a compromise between stability and absorbed energy is achieved.

V. Simulation and Experimental Results

The simulation results of the state-space model developed earlier are compared with that of a detailed model developed using MATLAB/SimPowerSystems and the results obtained from an experimental setup. The two inverters have been modeled as ideal voltage sources in Simulink as shown in Fig. 7. The simulation parameters are shown in Table II. A laboratory-scale microgrid, where the ac voltages and power ratings are scaled down by a factor of 10, was built. It consists of two DG units connected in parallel. Each DG is interfaced to the microgrid by a voltage-source inverter with *LCL* filter. The experimental setup is shown in Fig. 11. The setup parameters are listed in Table I. A circuit breaker is used to connect each unit to the PCC. Two Semikron SKAI IGBT blocks are used. The dSPACE 1103 control unit is used to implement and realize the proposed controller scheme in real time. The dSPACE interfacing board is equipped with eight analog to digital channels to interface the measured signals. The software code is generated by the real-time workshop under MATLAB/Simulink environment. The switching and sampling frequencies used are 10 and

TABLE II
SIMULATION AND EXPERIMENTAL PARAMETERS

Symbol	Description	Value
P_1^*	Active power set point for inverter 1	20 W
P_2^*	Active power set point for inverter 2	0 W
Q_1^*	Reactive power set point for inverter 1	0 VAR
Q_2^*	Reactive power set point for inverter 2	0 VAR
P_L	Load power	0
L_o	Inverter output inductance (small-signal and detailed simulation model)	2500 μH
k_ω	Frequency drooping gain	0.05 rad/s/W
k_a	Voltage drooping gain	0.01 V/W
V_o	Voltage set point	23 Vrms
f_o	Frequency set point	50 Hz
τ	Measurement filter time constant	0.1 s
V^*_{DClink}	Nominal dc-link voltage	40 V
$V^*_{\mathrm{DClink\_max}}$	Maximum dc-link voltage	120 V
m	Linearization factor relating V^2_{DClink} to V_{DClink}	0.0125

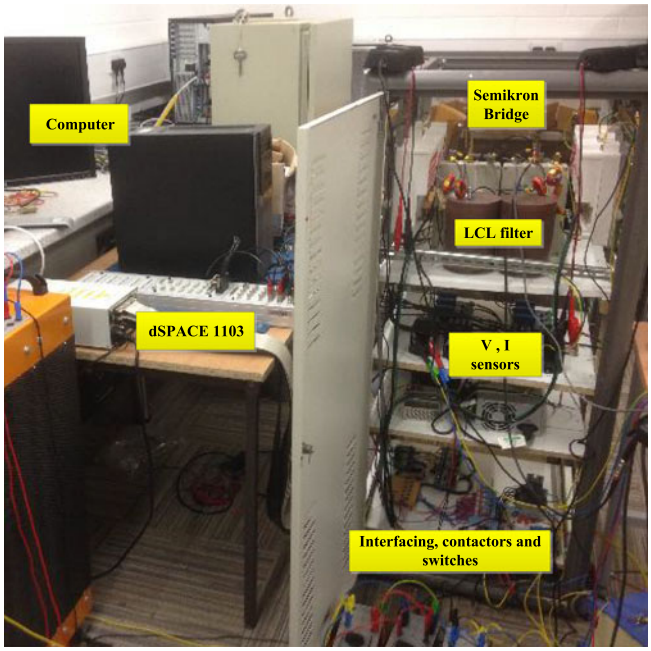

Fig. 11. View of the laboratory setup.

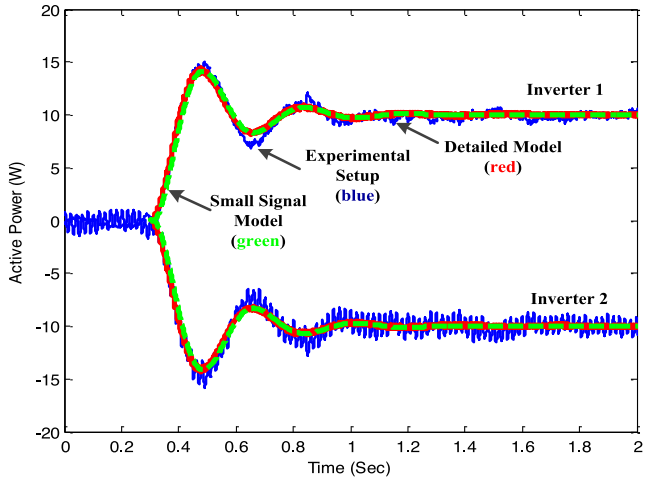

Fig. 12. Average measured active power of inverters 1 and 2 in island mode (case 1).

20 kHz, respectively. Because the ac voltages are scaled down, a step-up transformer is used on the grid side.

A. *Initial Conditions for the State-Space Model*

Two cases will be considered to validate the state-space model: In case 1, the two inverters are started in island mode with different power set points. Even though this case is not practical, as the supervisory controller should set the power set points equally before starting the inverters, it provides a good test for validating the small-signal model.

Case 2 represents unintentional islanding when the two inverters have different set points. Each state variable of the small-signal model described in (34) represents the deviation $\Delta x(t)$ from the equilibrium point x_{eq}. The time-domain response $x(t)$ is calculated by adding the deviation to the equilibrium point such as

$$x(t) = x_{\mathrm{eq}} + \Delta x(t). \tag{44}$$

The equilibrium points are calculated as follow: the average power equilibrium points are calculated using (7) and (8). The frequency equilibrium point is calculated using (6). The angle equilibrium point can be calculated using (45), which relates the active power transferred from each inverter to the load node

$$P_n = \frac{V_n V_L \sin(\theta_n)}{X}, n = 1, 2. \tag{45}$$

All equilibrium points are listed in Table III. The initial deviations from the equilibrium points $\Delta x(0)$ are calculated as

$$\Delta x(0) = x(0) - x_{\mathrm{eq}} \tag{46}$$

where $x(0)$ represents the initial condition at the beginning of the simulations. In case 1, $x(0)$ are the initial conditions before starting the inverters. In case 2, however, $x(0)$ represents the initial condition in grid-connected mode just before

TABLE III
EQUILIBRIUM POINTS AND INITIAL DEVIATIONS FOR THE SMALL-SIGNAL MODEL

State Variable	X_{eq}	Case 1 (starting in island mode)		Case 2 (unintentional islanding)	
		$X(0)$	$\Delta X(0)$	$X(0)$	$\Delta X(0)$
$\Delta\theta_1$	0.019 rad	0 rad	−0.019 rad	0.034 rad	0.015 rad
$\Delta\theta_2$	−0.019 rad	0 rad	0.019 rad	−0.004 rad	0.015 rad
$\Delta\omega_1$	314.66 rad/s	315.16 rad/s	0.5 rad/s	314.16 rad/s	−0.5 rad/s
$\Delta\omega_2$	314.66 rad/s	314.16 rad/s	–0.5 rad/s	314.16 rad/s	−0.5 rad/s
ΔV_1	23 Vrms	23 Vrms	0	23 Vrms	0
ΔV_2	23 Vrms	23 Vrms	0	23 Vrms	0
ΔP_{avg1}	10W	0	−10 W	20 W	10 W
ΔP_{avg2}	−10W	0	10 W	0 W	10 W
ΔQ_{avg1}	0	0	0	0	0
ΔQ_{avg2}	0	0	0	0	0

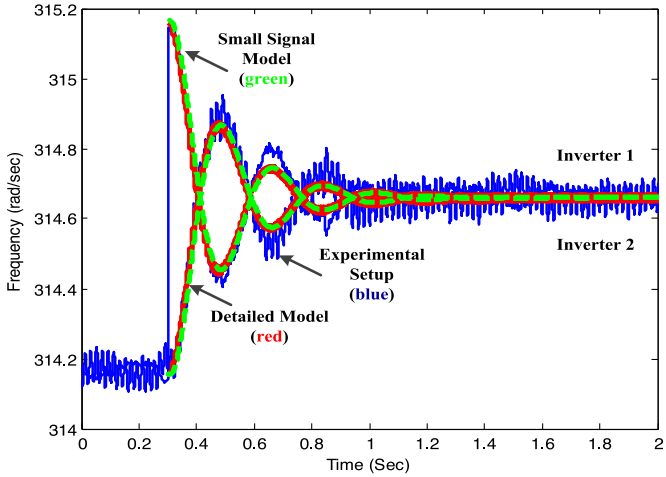

Fig. 13. Frequency of inverters 1 and 2 in island mode (case 1).

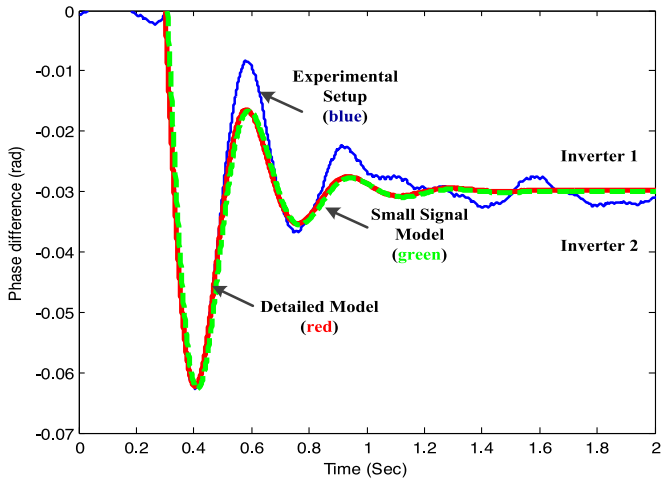

Fig. 14. Phase of inverters 1 and 2 in island mode (case 1).

unintentional islanding. All the initial conditions and initial deviations are calculated for both cases and listed in Table III.

B. Validation of the Small-Signal Model

1) Results of Case 1: Fig. 12 depicts the average active power for both inverters under case 1 conditions. The figure includes the results obtained from the small-signal model, the detailed Simulink model and the experimental setup. As can be seen, the small-signal model is in complete agreement with the detailed model and both agree with the experimental results. A similar conclusion can be obtained from Figs. 13 and 14, which show the response of the frequency and phase angle, respectively.

2) Results of Case 2: In this case, the two inverters are initially operating in grid-connected mode. At time $t = 2.1$ s, the grid is isolated so the two inverters operate in island mode. Fig. 15 shows the responses of the average active power (instantaneous power after being filtered by the LPF) of both inverters using the detailed and the small-signal model and the experimantal setup.

Again, the theoretical and experimental results are all in full agreement. Fig. 15 also shows the frequency responses of both inverters. The behavior of the second inverter, which is importing 10 W, develops high voltage across the dc-link capacitor resulting in a power trip as shown in Fig. 16, which depicts the experimental dc-link voltage of inverter 2 before and after islanding. When the dc link exceeds the max limit, a trip signal is generated.

C. Results of the Proposed DC Controller

Fig. 17 shows the simulation and experimental results of the unintentional islanding case (case 2) with $P_L = 0$. The first inverter was generating 20 W, while the second inverter was generating 0 W in grid-connected mode. When the islanding occurs at $t = 3$ s, the output powers become $P_1 = 10$ W and $P_2 = -10$ W, which agree with (7) and (8). The dc-link voltage of inverter 2 starts to rise, and when it reaches 100 V the dc-link controller is activated. The active powers are then reduced to zero and the dc voltage is reduced to 60 V. The charging time in simulation and practical results are slightly different due the dynamics of the practical dc source (applied on the dc-link capacitor), the simulation and the theoretical calculations assume ideal sources and the discussion of this is beyond the scope of this paper. The effectiveness of the proposed controller is clear, as it has prevented the dc-link voltage from reaching the trip limit by quickly adjusting the power demand and the inverters

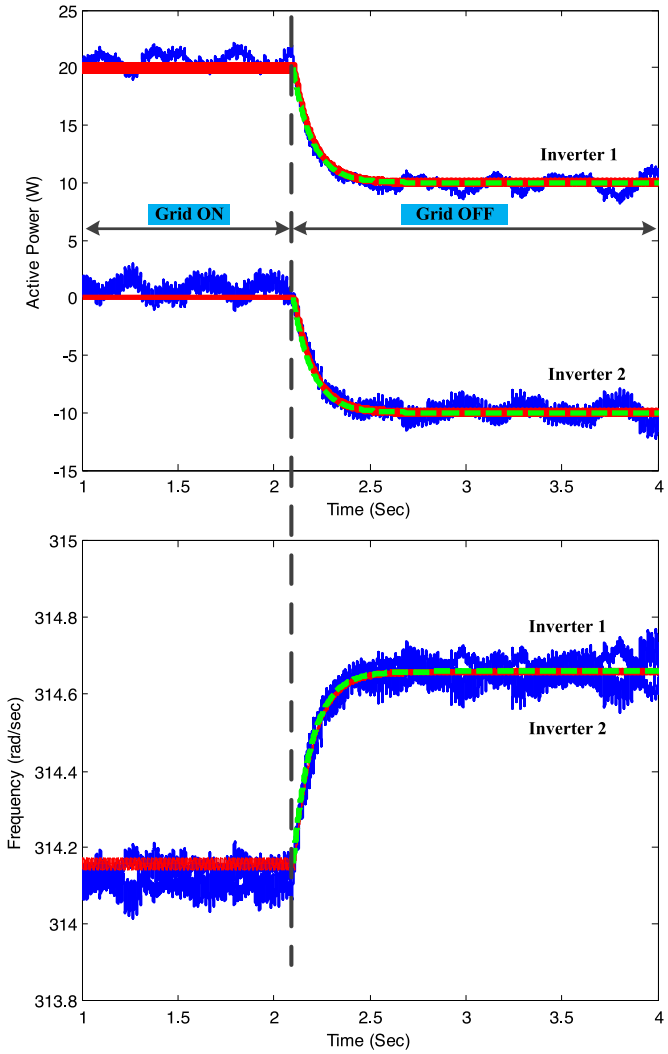

Fig. 15. Average measured active power (above) and frequency (below) of inverters 1 and 2 after grid loss—unintentional islanding (case 2).

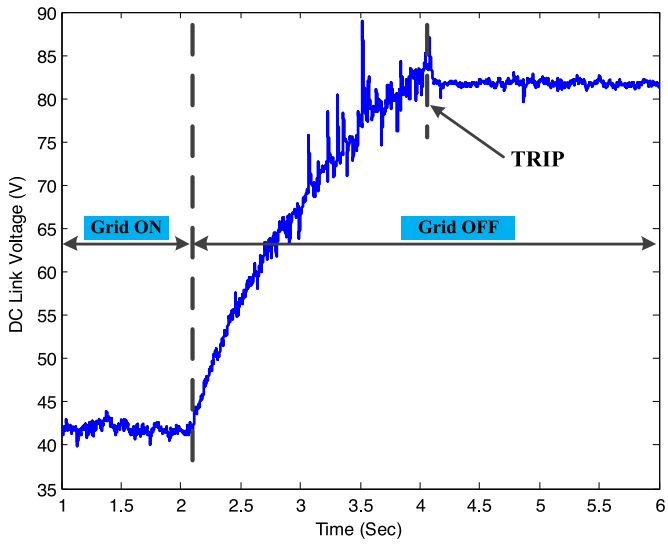

Fig. 16. DC-link voltage across the capacitor of inverter 2.

kept working waiting for an update signal to be received from the supervisory controller.

According to the eigenvalues of the dc-link controller of Fig. 10, the predicted transient response of the dc voltage is $c(t) = e^{-2.6t}\sin(2\pi 3.7t)$. The magnified portion in Fig. 17 shows the transient oscillation of the dc voltage. The oscillation frequencies of the detailed model and the experimental setup are 3.57 and 3.125 Hz, respectively. The small-signal model has provided good prediction of the transient response. The exponential decaying term also agrees with the eigenvalues of Fig. 10.

To test the controller at high voltages and power, Fig. 18 shows the simulation results of unintentional islanding of two inverters operating at high voltages (nominal ac voltage $V_o = 230$ Vrms and nominal dc-link voltage $V^*_{\mathrm{DClink}} = 400$ V). Controllers' parameters have been scaled according to this voltage level. One inverter was injecting 10 kW and the second inverter was injecting 0 kW into the grid before islanding. The simulation is carried out for two different values of dc-link capacitance (2200 μF and 4400 μF). As expected from (38), the dc-link voltage peak deviation is inversely proportional to the capacitance value, but in both cases, the controller was able to prevent the dc-link voltage from reaching the trip limit of 1000 V. The response with the low value of dc-link capacitance is quite oscillatory. Choosing a larger capacitance value will give better transient response but it will also increase cost. Choosing a smaller capacitance value can either lead to instability (if a high k_{DC} value is used) or inverter shutdown by the overvoltage protection system. It is worth mentioning here that the dc-link capacitance value has traditionally been selected to satisfy certain requirements such as filtering rectifier output ripple. However, if the inverter is to be used in a microgrid, the effect of unintentional islanding on the rise of the dc-link voltage needs to be taken into account when selecting the dc-link capacitance. The analysis method and the controller proposed in this paper can assist the designer in choosing the required value of dc-link capacitance. The small-signal model can be used to first evaluate the rise in the dc-link voltage during unintentional islanding (using the original value of dc-link capacitance) and second to select a suitable value of k_{DC}.

If a compromise between the stability and limiting dc-link voltage could not be reached, and hence, the proposed controller is not able to prevent the dc-link voltage from reaching its trip limit with acceptable transient performance, an increase in the dc-link capacitance becomes essential. The designer then needs to increase the dc-link capacitance just enough to give a safe performance during unintentional islanding. The root locus graph can be used to optimize the selection of the dc-link capacitance and the controller gain k_{DC}.

VI. Conclusion

This paper has investigated the transient power between the paralleled inverter during unintentional islanding and a controller to limit this circulating power has been proposed. The controller monitors the dc-link voltage and if the voltage rises above a specific limit, due to power being imported, the con-

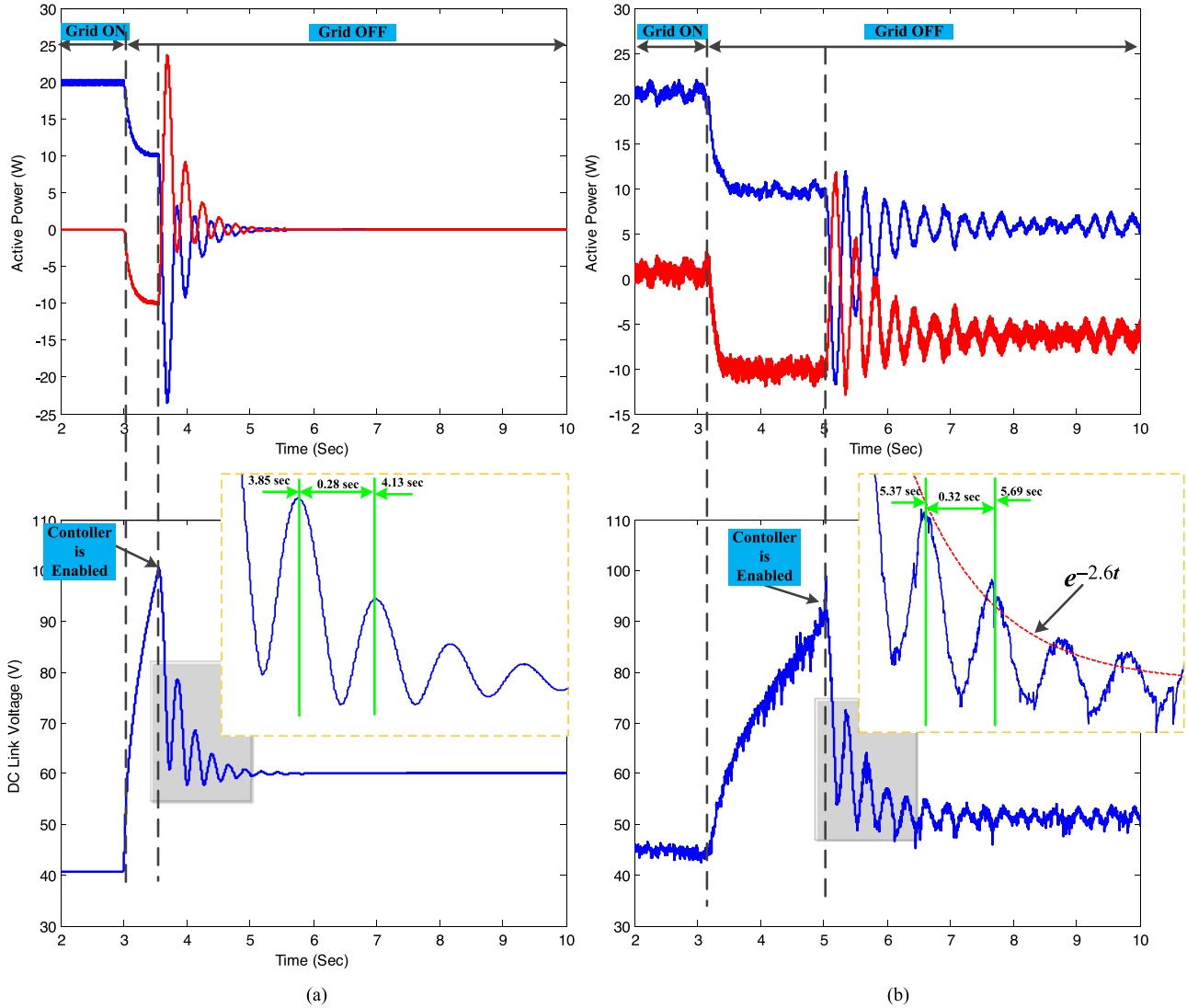

Fig. 17. Average measured active power of both inverters and dc-link voltage of inverter 2 with the proposed controller ($k_{\mathrm{DC}} = 1$). (a) Simulink detailed model, (b) experimental setup.

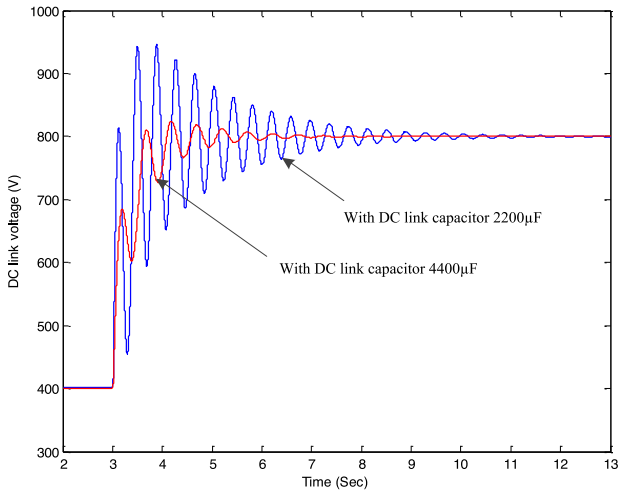

Fig. 18. Dc-link voltage responses in case of different values of dc-link capacitor.

troller adjusts the power set point in proportion to the rise in the voltage. A small-signal model of a microgrid consisting of two inverters in island mode has been developed and used to design the controller. Simulation and experiments confirmed the accuracy of the developed model and the validity of the design.

Appendix A
State-Space Equations Coefficients

$$a_1 = \frac{\partial P_1}{\partial V_1} = \frac{2\frac{X}{R}V_{1\mathrm{eq}} + 2V_{2\mathrm{eq}}\sin(\theta_{1\mathrm{eq}} - \theta_{2\mathrm{eq}}) + \frac{X}{R}V_{2\mathrm{eq}}\cos(\theta_{1\mathrm{eq}} - \theta_{2\mathrm{eq}})}{M}$$

$$b_1 = \frac{\partial P_1}{\partial V_2} = \frac{2V_{1\mathrm{eq}}\sin(\theta_{1\mathrm{eq}} - \theta_{2\mathrm{eq}}) + \frac{X}{R}V_{1\mathrm{eq}}\cos(\theta_{1\mathrm{eq}} - \theta_{2\mathrm{eq}})}{M}$$

$$
\begin{aligned}
c_1 &= \frac{\partial P_1}{\partial \theta_1} \\
&= \frac{2V_{1\mathrm{eq}}V_{2\mathrm{eq}}\cos(\theta_{1\mathrm{eq}}-\theta_{2\mathrm{eq}}) - \frac{X}{R}V_{1\mathrm{eq}}V_{2\mathrm{eq}}\sin(\theta_{1\mathrm{eq}}-\theta_{2\mathrm{eq}})}{M} \\
d_1 &= \frac{\partial P_1}{\partial \theta_2} = -c_1 \\
a_2 &= \frac{\partial P_2}{\partial V_1} \\
&= \frac{2V_{2\mathrm{eq}}\sin(\theta_{2\mathrm{eq}}-\theta_{1\mathrm{eq}}) + \frac{X}{R}V_{2\mathrm{eq}}\cos(\theta_{2\mathrm{eq}}-\theta_{1\mathrm{eq}})}{M} \\
b_2 &= \frac{\partial P_2}{\partial V_2} \\
&= \frac{2\frac{X}{R}V_{2\mathrm{eq}} + 2V_{1\mathrm{eq}}\sin(\theta_{2\mathrm{eq}}-\theta_{1\mathrm{eq}}) + \frac{X}{R}V_{1\mathrm{eq}}\cos(\theta_{2\mathrm{eq}}-\theta_{1\mathrm{eq}})}{M} \\
c_2 &= \frac{\partial P_2}{\partial \theta_1} \\
&= \frac{-2V_{1\mathrm{eq}}V_{2\mathrm{eq}}\cos(\theta_{2\mathrm{eq}}-\theta_{1\mathrm{eq}}) + \frac{X}{R}V_{1\mathrm{eq}}V_{2\mathrm{eq}}\sin(\theta_{2\mathrm{eq}}-\theta_{1\mathrm{eq}})}{M} \\
d_2 &= \frac{\partial P_2}{\partial \theta_2} = -c_2 \\
a_3 &= \frac{\partial Q_1}{\partial V_1} \\
&= \frac{2\left(\frac{X^2}{R^2}+2\right)V_{1\mathrm{eq}} - 2V_{2\mathrm{eq}}\cos(\theta_{1\mathrm{eq}}-\theta_{2\mathrm{eq}}) + \frac{X}{R}V_{2\mathrm{eq}}\sin(\theta_{1\mathrm{eq}}-\theta_{2\mathrm{eq}})}{M} \\
b_3 &= \frac{\partial Q_1}{\partial V_2} \\
&= \frac{-2V_{1\mathrm{eq}}\cos(\theta_{1\mathrm{eq}}-\theta_{2\mathrm{eq}}) + \frac{X}{R}V_{1\mathrm{eq}}\sin(\theta_{1\mathrm{eq}}-\theta_{2\mathrm{eq}})}{M} \\
c_3 &= \frac{\partial Q_1}{\partial \theta_1} \\
&= \frac{2V_{1\mathrm{eq}}V_{2\mathrm{eq}}\sin(\theta_{1\mathrm{eq}}-\theta_{2\mathrm{eq}}) + \frac{X}{R}V_{1\mathrm{eq}}V_{2\mathrm{eq}}\cos(\theta_{1\mathrm{eq}}-\theta_{2\mathrm{eq}})}{M} \\
d_3 &= \frac{\partial Q_1}{\partial \theta_2} = -c_3 \\
a_4 &= \frac{\partial Q_2}{\partial V_1} \\
&= \frac{-2V_{2\mathrm{eq}}\cos(\theta_{2\mathrm{eq}}-\theta_{1\mathrm{eq}}) + \frac{X}{R}V_{2\mathrm{eq}}\sin(\theta_{2\mathrm{eq}}-\theta_{1\mathrm{eq}})}{M} \\
b_4 &= \frac{\partial Q_2}{\partial V_2} \\
&= \frac{2\left(\frac{X^2}{R^2}+2\right)V_{2\mathrm{eq}} - 2V_{1\mathrm{eq}}\cos(\theta_{2\mathrm{eq}}-\theta_{1\mathrm{eq}}) + \frac{X}{R}V_{1\mathrm{eq}}\sin(\theta_{2\mathrm{eq}}-\theta_{1\mathrm{eq}})}{M} \\
c_4 &= \frac{\partial Q_2}{\partial \theta_1} \\
&= \frac{-2V_{1\mathrm{eq}}V_{2\mathrm{eq}}\sin(\theta_{2\mathrm{eq}}-\theta_{1\mathrm{eq}}) - \frac{X}{R}V_{1\mathrm{eq}}V_{2\mathrm{eq}}\cos(\theta_{2\mathrm{eq}}-\theta_{1\mathrm{eq}})}{M} \\
d_4 &= \frac{\partial Q_2}{\partial \theta_2} = -c_4
\end{aligned}
$$

where $M = 4X + \frac{X^3}{R^2}$.

$$
[\mathrm{A}_1] = \begin{bmatrix}
0 & 1 & 0 & 0 & 0 & 0 & 0 & 0 & 0 & 0 \\
0 & 0 & 0 & 1 & 0 & 0 & 0 & 0 & 0 & 0 \\
-\frac{k_\omega.c_1}{\tau} & -\frac{k_\omega.d_1}{\tau} & -\frac{1}{\tau} & 0 & -\frac{k_\omega.a_1}{\tau} & -\frac{k_\omega.b_1}{\tau} & 0 & 0 & 0 & 0 \\
-\frac{k_\omega.c_2}{\tau} & -\frac{k_\omega.d_2}{\tau} & 0 & -\frac{1}{\tau} & -\frac{k_\omega.a_2}{\tau} & -\frac{k_\omega.b_2}{\tau} & 0 & 0 & 0 & 0 \\
-\frac{k_a.c_3}{\tau} & -\frac{k_a.d_3}{\tau} & 0 & 0 & -\frac{(1+k_a.a_3)}{\tau} & -\frac{k_a.b_3}{\tau} & 0 & 0 & 0 & 0 \\
-\frac{k_a.c_4}{\tau} & -\frac{k_a.d_4}{\tau} & 0 & 0 & -\frac{k_a.a_4}{\tau} & -\frac{(1+k_a.b_4)}{\tau} & 0 & 0 & 0 & 0 \\
\frac{c_1}{\tau} & \frac{d_1}{\tau} & 0 & 0 & \frac{a_1}{\tau} & \frac{b_1}{\tau} & \frac{-1}{\tau} & 0 & 0 & 0 \\
\frac{c_2}{\tau} & \frac{d_2}{\tau} & 0 & 0 & \frac{a_2}{\tau} & \frac{b_2}{\tau} & 0 & \frac{-1}{\tau} & 0 & 0 \\
\frac{c_3}{\tau} & \frac{d_3}{\tau} & 0 & 0 & \frac{a_3}{\tau} & \frac{b_3}{\tau} & 0 & 0 & \frac{-1}{\tau} & 0 \\
\frac{c_4}{\tau} & \frac{d_4}{\tau} & 0 & 0 & \frac{a_4}{\tau} & \frac{b_4}{\tau} & 0 & 0 & 0 & \frac{-1}{\tau}
\end{bmatrix}
$$

$$
[\mathrm{A}_3] = \begin{bmatrix}
\frac{2mc_1}{C_{dc}} & \frac{2md_1}{C_{dc}} & 0 & 0 & \frac{2ma_1}{C_{dc}} & \frac{2mb_1}{C_{dc}} & 0 & 0 & 0 & 0 & 0 & 0 & 0 & 0 \\
\frac{2mc_2}{C_{dc}} & \frac{2md_2}{C_{dc}} & 0 & 0 & \frac{2ma_2}{C_{dc}} & \frac{2mb_2}{C_{dc}} & 0 & 0 & 0 & 0 & 0 & 0 & 0 & 0
\end{bmatrix}
$$

APPENDIX B
COMPLETE STATE-SPACE MODEL

[A1] and [A3] as shown at the bottom of the previous page.

REFERENCES

[1] R. Tirumala, N. Mohan, and C. Henze, "Seamless transfer of grid-connected PWM inverters between utility-interactive and stand-alone modes," in *7th Annu. IEEE Appl. Power Electron. Conf. Expo.*, Dallas, TX, USA, 2002, pp. 1081–1086.

[2] F. S. Pai and S. J. Huang, "A novel design of line-interactive uninterruptible power supplies without load current sensors," *IEEE Trans. Power Electron.*, vol. 21, no. 1, pp. 202–210, Jan. 2006.

[3] H. Tao, J. L. Duarte, and M. A. M. Hendrix, "Line-interactive UPS using a fuel cell as the primary source," *IEEE Trans. Ind. Electron.*, vol. 55, no. 8, pp. 3012–3021, Jul. 2008.

[4] M. A. P. de Azpeitia, A. Fernández, D. G. Lamar, M. Rodriguez, and M. M. Hernando, "Simplified voltage-sag filler for line-interactive uninterruptible power supplies," *IEEE Trans. Ind. Electron.*, vol. 55, no. 8, pp. 3005–3011, Aug. 2008.

[5] H. Kim, T. Yu, and S. Choi, "Indirect current control algorithm for utility interactive inverters in distributed generation systems," *IEEE Trans. Power Electron.*, vol. 23, no. 3, pp. 1342–1347, May 2008.

[6] W. J. Ho, J. B. Lio, and W. S. Feng, "A line-interactive UPS structure with built-in vector-controlled charger and PFC," in *Proc. Int. Conf. Power Electron. Drive Syst.*, 1997, pp. 127–132.

[7] Y. Okui, S. Ohta, N. Nakamura, H. Hirata, and M. Yanagisawa, "Development of line interactive type UPS using a novel control system," in *Proc. 25th Int. Telecommun. Energy Conf.*, Yokohama, Japan, 2003, pp. 796–801.

[8] M. C. Chandorkar, D. M. Divan, and R. Adapa, "Control of parallel connected inverters in standalone ac supply systems," *IEEE Trans. Ind. Appl.*, vol. 29, no. 1, pp. 136–143, Aug. 1993.

[9] J. M. Guerrero, J. C. Vasquez, J. Matas, L. G. de Vicuña, and M. Castilla, "Hierarchical control of droop-controlled AC and DC microgrids—A general approach toward standardization," *IEEE Trans. Ind. Electron.*, vol. 58, no. 1, pp. 158–172, Jan. 2011.

[10] *IEEE Standard for Interconnecting Distributed Resources with Electric Power Systems*, IEEE Standard 1547, p. 16, 2003.

[11] M. Abusara, J. M. Guerrero, and S. Sharkh, "Line interactive UPS for microgrids," *IEEE Trans. Ind. Electron.*, vol. 61, no. 3, pp. 1292–1300, Mar. 2014.

[12] F. Luo, Y. Lai, C. K. Tse, and K. Loo, "A triple-droop control scheme for inverter-based microgrids," in *Proc. IEEE 38th Annu. Conf. Ind. Electron. Soc.*, 2012, pp. 3368–3375.

[13] Y. R. Mohamed, H. H. Zeineldin, M. Salama, and R. Seethapathy, "Seamless formation and robust control of distributed generation microgrids via direct voltage control and optimized dynamic power sharing," *IEEE Trans. Power Electron.*, vol. 27, no. 3, pp. 1283–1294, Mar. 2012.

[14] H. Tao, J. L. Duarte, and M. A. Hendrix, "Line-interactive UPS using a fuel cell as the primary source," *IEEE Trans. Ind. Electron.*, vol. 55, no. 8, pp. 3012–3021, Jul. 2008.

Walid R. Issa received the B.Sc. and M.Sc. degrees in electrical engineering from the Islamic University of Gaza (IUG), Gaza, Palestine, in 2007 and 2011, respectively. He is currently working toward the Ph.D. degree at University of Exeter, Penryn, U.K.

He worked as a Teaching Assistant at IUG, during 2007–2010. In addition, he was a Lecturer at the University College of Applied Science, Gaza, during 2009–2011. His main research interests include power electronics, digital control, dc/ac converters, and microgrids.

Mohammad A. Abusara received the B.Eng. degree from Birzeit University, Birzeit, Palestine, in 2000, and the Ph.D. degree from the University of Southampton, Southampton, U.K., in 2004, both in electrical engineering.

He is currently a Senior Lecturer in Renewable Energy, University of Exeter, Penryn, U.K. He has more than ten years of industrial experience with Bowman Power Group, Southampton, in the field of research and development of digital control of power electronics. During his years in industry, he designed and prototyped a number of commercial products that include grid and parallel connected inverters, microgrid, dc/dc converters for hybrid vehicles, and sensorless drives for high-speed permanent magnet machines.

Suleiman M. Sharkh (M'13) obtained the B.Eng. and Ph.D. degrees in electrical engineering from the University of Southampton, Southampton, U.K., in 1990 and 1994, respectively.

He is currently a Professor of power electronics, machines and drives and the Head of the Electromechanical Research Group, University of Southampton. He is also the Managing Director of HiT Systems Ltd. and a Director of HiT Power Ltd. He has published more than 140 papers in academic journals and conferences.

Prof. Sharkh is a Member of the IET and a Chartered Engineer. He received the Engineer Energy Innovation Award for his work on rim-driven thrusters and marine turbine generators in 2008.